7-1-2016

IDENTIFYING SAND BLOW VENTS AND OTHER SUBSURFACE GEOLOGICAL FEATURES USING GROUND PENETRATING RADAR AND ELECTRICAL RESISTIVITY

Trevor Thomas Satterfield

IDENTIFYING SAND BLOW VENTS AND OTHER SUBSURFACE GEOLOGICAL FEATURES USING GROUND PENETRATING RADAR AND ELECTRICAL RESISTIVITY

by

Trevor Thomas Satterfield

A Thesis

Submitted in Partial Fulfillment of the

Requirements for the Degree of

Master of Science

Major: Earth Sciences

The University of Memphis

July 21, 2016

Abstract

Satterfield, Trevor Thomas. M.S. The University Of Memphis. August, 2016. Identifying Sand Blow Vents And Other Subsurface Geological Features Using Ground Penetrating Radar And Electrical Resistivity. Major Professor: Christine A. Powell, Ph.D.

Aerial photographs suggest the presence of numerous sand blows in southern Arkansas but few of the sites have been investigated. Limited work involving trenching, conductivity surveys, and cone penetration tests verify the presence of sand blows in two locations, Ashley County and Desha County. A third location in Lincoln County, called the Phenix site, has received little attention. In this study, ground penetrating radar (GPR) and electrical resistivity survey (ER) have been used to investigate sand blow vents at the Morgan site located in Ashley County and at the Phenix site. Nine sand blow vents were detected in total but wet weather conditions diminished data quality at the Phenix site, illustrating the advantage of conducting surveys under dry conditions. Use of GPR and ER removes most of the guesswork involved in detecting and documenting the presence of sand blows and reduces the time and expense involved in experimental trenching.

Table of Contents

Table of Figures

1. Introduction

During earthquakes there are times of sever shaking, which create conditions for liquefaction features like sand blows. Sand blows are formed when the seismic wave train of the earthquake passes through a wet sandy layer, forcing the sand grains to compact, and increasing the pore pressure. As the duration of the shaking increase, so does the pore pressure until it overcomes the overburden pressure, allowing the wet sand to rise to the surface through holes or cracks in the overlying layer. The visible result is a dome shape formation of wet sand on the surface (Al-Shukri et al., 2005).

Documenting the presence of sand blows and other liquefaction features is needed to better understand the paleoseismic history of the region. In order to do this, trenches and cone penetration tests are used to divulge lateral variations and soil layers. However, each trench takes about a week to complete and each cone penetration test takes multiple hours to perform. An additional downside is the negative environmental effect of leaving behind a trench or hole. Therefore, using geophysical surveys at suspected sand blow locations would not only provide direct observations at depth but also save time, money and drastically cut down on the guesswork involved in defining locations to trench.

2. Previous Work

Previous studies have been conducted in a few sites of central and southeastern Arkansas documenting sand blows. Sand blows have been observed on aerial photographs of central and southern Arkansas near Montrose (Cox, 2002; Cox and Larsen, 2004; Cox et al., 2004a; Al-Shukri et al., 2005, Cox et al., 2007) (Figure 1). Three sites, the Morgan site, the Golden site and the Phenix site, are of particular interest due to the large number of sand blow features present (Figure 2). The sand blows are

probably too far away from the New Madrid seismic zone (NMSZ) to be attributed to the large 1811-1812 earthquakes or older large events in the NMSZ (Cox et al., 2007); the presence of the sand blows implies that additional, large earthquakes occurred to the south of the NMSZ but the seismic source location is unknown.

Figure 1: Map showing the sites used in the study. (made using Google Earth) geophysics. Rhombus: Golden site used in Cox et al. (2007); Triangles: sites used in Al-Shukri et al. (2005); Circle: site used in Wolf et al. (1998). (made using Google Earth)

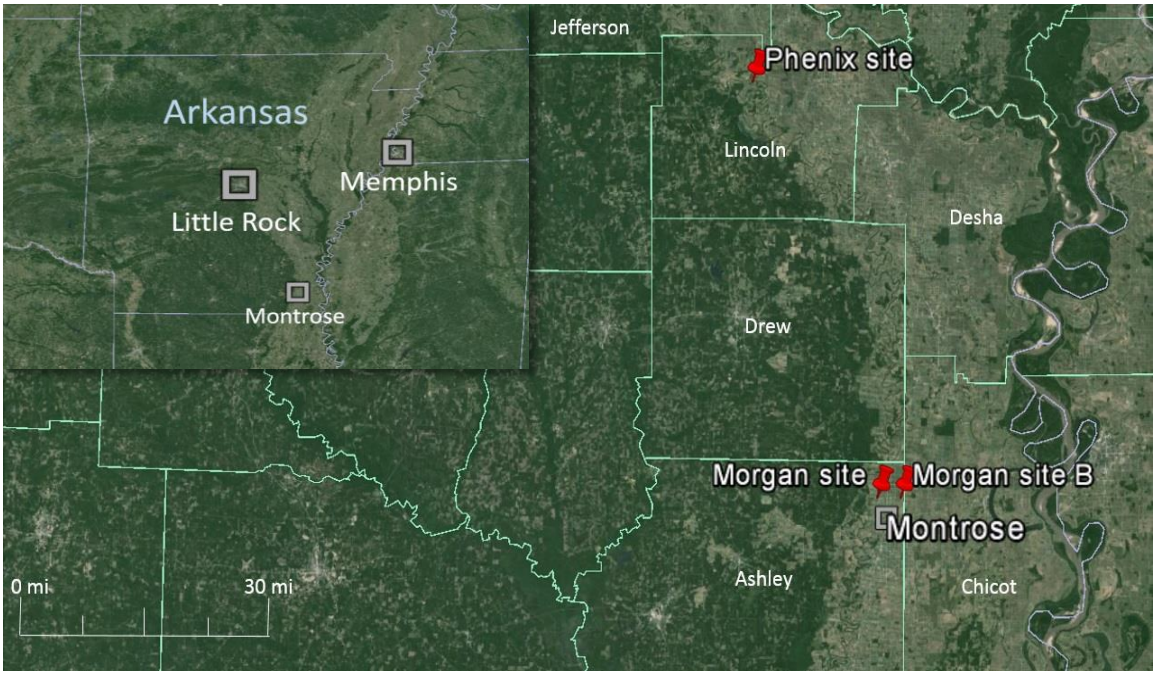

Figure 2: Map showing the sites used in the study. (made using Google Earth)

To date, electrical conductivity surveys were conducted at suspected sand blow sites in the three southern Arkansas counties (Ashley, Desha, and Lincoln) and trenching was done at the Ashley and Desha counties (Cox et al., 2007). The electrical conductivity survey done at the Morgan site in Ashley county revealed two circular areas of high conductivity believed to be sand blow vents; the trenching done at the same location revealed alternatively dipping clay and sand layers at the sand blow vents. In addition, cone penetration tests were conducted by the U.S. Geological Survey at the Morgan and Golden sites, which revealed alternating layers of liquefiable sand and clay (Cox et al., 2007).

Studies have been conducted using ground penetrating radar (GPR) and electromagnetic resistivity (ER) survey to investigate sand blows. Wolf et al. (1998) used ER and electromagnetic induction to identify the sand feeder dike in a sand blow

associated with the New Madrid seismic zone (Figure 1). This study is promising but the approach, using a Wenner array, provided limited depth resolution.

Al-Shukri et al. (2005) imaged sand blows in the western lowlands of the Mississippi Embayment in central Arkansas (Figure 1). They were successful in imaging a sand feeder dike using a 400 MHz GPR antenna, which was confirmed by trenching (Tuttle et al, 2006) (Figure 3).

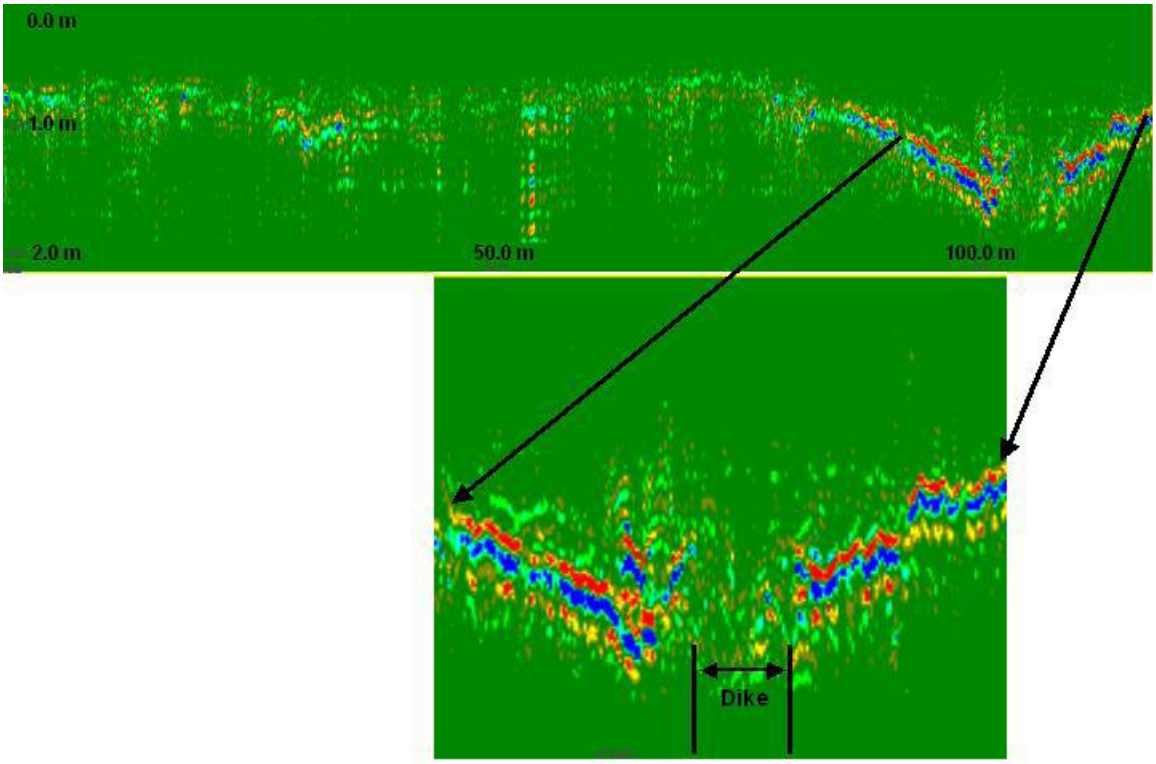

Figure 3: Example of a sand feeder dike imaged by GPR. (Al-Shukri et al., 2005)

3. **Geology of the Region**

In order to speculate upon an alternative seismic source location for the observed sand blows in the study area, some background geology for southern Arkansas must be described. The super continent of Rodinia was breaking apart in late Precambrian time and the Iapetus Ocean began to form. This produced multiple zigzag sections of intersecting transform faults and rift segments that stretched up the east coast. A couple of key tectonic features resulted during this time that affected my study area. These are the Alabama-Oklahoma (AL-OK) transform fault reaching from present day Alabama to Oklahoma, and the Mississippi Valley graben system consisting of rift-related faults that propagated into the continent (Thomas, 2006). The AL-OK transform fault marks the southern end of the Mississippi graben system.

Closure of the Iapetus Ocean and formation of the super continent Pangea occurred by Permian time. As a consequence of the closure, the Ouachita thrust belt covered the AL-OK transform and extended into Arkansas. The Ouachita Mountains were eroded between the Permian and Jurassic and are covered by Mesozoic and Cenozoic sediments (Thomas, 2006). Conceivably, the heavily faulted crust could have reactivated producing an earthquake large enough to create sand blows in southern Arkansas.

4. Geophysical Sites

Three locations were investigated. Site locations and field conditions at the time of the survey are indicated in Table 1. The first location is north of Montrose, Arkansas (Figure 2).

Table 1: Site locations and field conditions at the time of the survey.

Sites	GPS Locations	Site Conditions
Morgan site	33°19'59.16"N 91°29'44.50"W	Dry, no grass but has crops
Phenix site	34° 1'26.51"N 91°46'0.74"W	Very wet, no vegetation
Morgan site B	33°19'50.15"N 91°27'13.05"W	Dry, some patches of grass

This location is the Morgan site analyzed by Cox et al. (2007). At this location three 164 meter long resistivity lines were deployed to profile the site. Fifty GPR profiles were collected using a separation of 5 meters to further profile the site. The initial site area was a 100 by 150 meter rectangle as opposed to the 100 by 100 by 140 meter triangle used by Cox et al. (2007) (Figure 4).

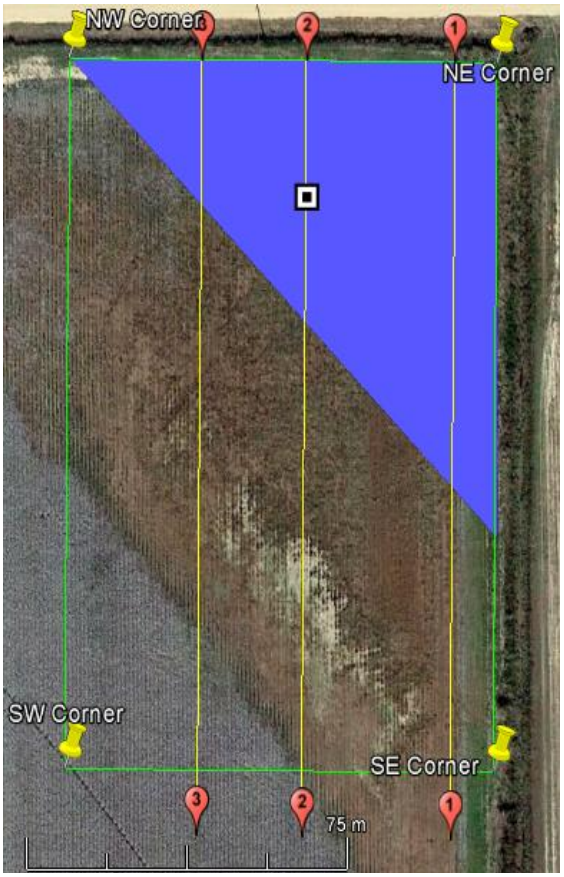

Figure 4: Location of the three resistivity lines. Rectangle is 100 by 150 meters. The white square represents the location of the trench from Cox et al. (2007). Blue triangle marks the conductivity study by Cox et al. (2007). (made using Google Earth)

Figure 5: Same as Figure 4 showing the resistivity lines used for the 3-D image within the 100 by 150 meter rectangle. (made using Google Earth)

A smaller area of 9 x 42 meters was chosen inside the initial site area for further analysis because it is a sandy area and thus an excellent target for a sand blow feature (Figure 5). Nine 42 meter long resistivity lines were deployed within the smaller study area (Figure 5) and the data were used to form a 3-D ER image. In addition, nine GPR lines were collected over the 3-D ER area. These lines were 41 meters in length and were separated by 1 meter. The data collected at site 1 was used to establish appropriate ER

and GPR parameters to locate sand blow features at the other sites where trenching was not conducted.

The second location investigated was the Phenix site (Figure 2). This area has not been trenched but aerial photographs suggest possible sand blows at the site. The grid covered an area of 9 by 41 meters (Figure 6). 2-D resistivity lines were created and the data used to develop a 3-D resistivity image (Figure 6). Ten 41 meter long GPR surveys were taken over the same area (Figure 7).

Figure 6: Location of the ER and GPR lines at the Phenix site. (made using Google Earth)

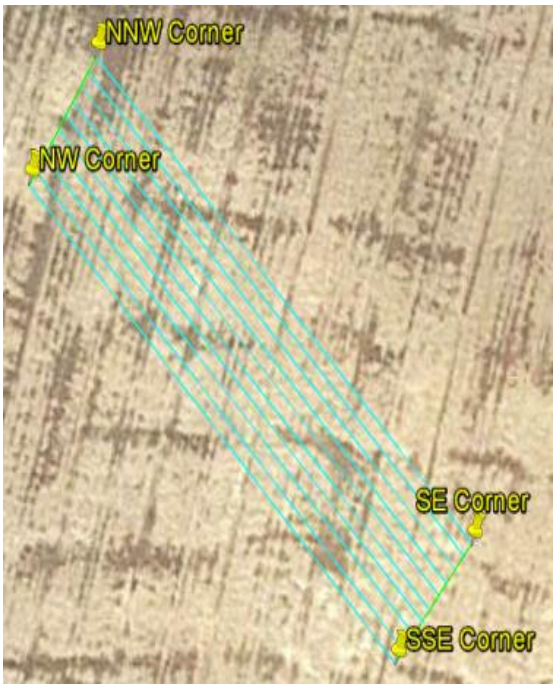

Figure 7: The 10 overlapping GPR surveys. (made using Google Earth)

The third location investigated was called the Morgan site B. This location is important because although it does not contain sand blows, a stream lineament suggests it

could contain a fault that served as the source zone for the liquefaction features in the area. Two 400 m GPR lines were run at the site along farm roads (Figure 8).

Figure 8: The two 400 meter long GPR lines at Morgan site B. The red line is the data section displayed below (made using Google Earth)

5. Equipment/Software

5.1 GPR

GPR is used to view the shallow subsurface in much the same way as seismic reflection surveys. The GPR antennas transmit high frequency radio waves (10 MHz to 1GHz) into the ground. These radio waves will either reflect or refract when the energy encounters material with different dielectric constants. If there is a sharp contrast then the wave will be reflected. If there is a significant boundary contrast in multiple layers then the wave will attenuate more quickly. In southern Arkansas the water table is 2-3 meters deep and there are multiple clay layers. This creates a problem using GPR because as the radio wave passes through the earth and encounters the clay layers and water, the signal strength will decrease sharply. This reduces the maximum imaging depth of the GPR and it also decreases the imaging resolution.

The GPR equipment that was used is the ProEx series from MALA (www.malags.com). 100 and 250 MHz antennas were employed. The maximum

penetration depths are expected to be 9 meters and 20 meters for the 250 MHz antenna and the 100 MHz antenna, respectively (www.malags.com). The maximum resolution is 0.6 meter and 1.5 meters for the 250 MHz antenna and that the 100 MHz antenna, respectively (www.malags.com). The 100 MHz antenna was pulled with a counting wheel attached to it and the 250 MHz antenna was sitting inside a push cart that has a counting rear wheel.

The data was processed using RadExplorer 1.42 (www.malags.com) and a simple built in program called GroundVision 2 (www.malags.com). GroundVision 2 is quick and easy to use for gathering data in the field. It has simple processing tools like signal amplification, background filtering and changing color schemes. RadExplorer 1.4 has more capabilities than the built-in program. Some processing routines that the user has access to include: DC removal, Time Adjustment, Spatial Interpolation, Background Removal, Amplitude Correction, Bandpass Filtering and Topographic Correction. These processing routines are not used in the field.

5.2 Electrical Resistivity

The Electrical Resistivity surveys were executed using SuperSting R8/IP equipment (www.agiusa.com) and a dipole-dipole array (Figure 9). Each resistivity line used had either 84 or 42 electrodes to take measurements that were 163 meters and 41 meters in length, respectively. In each survey the pseudoresisitvity measurements used two coordinates (x,z) to describe an electrode location. In figure 9 the pseudoresistivity measurement is referred to as the pseudosection plot point. These measurements make up each 2-D survey.

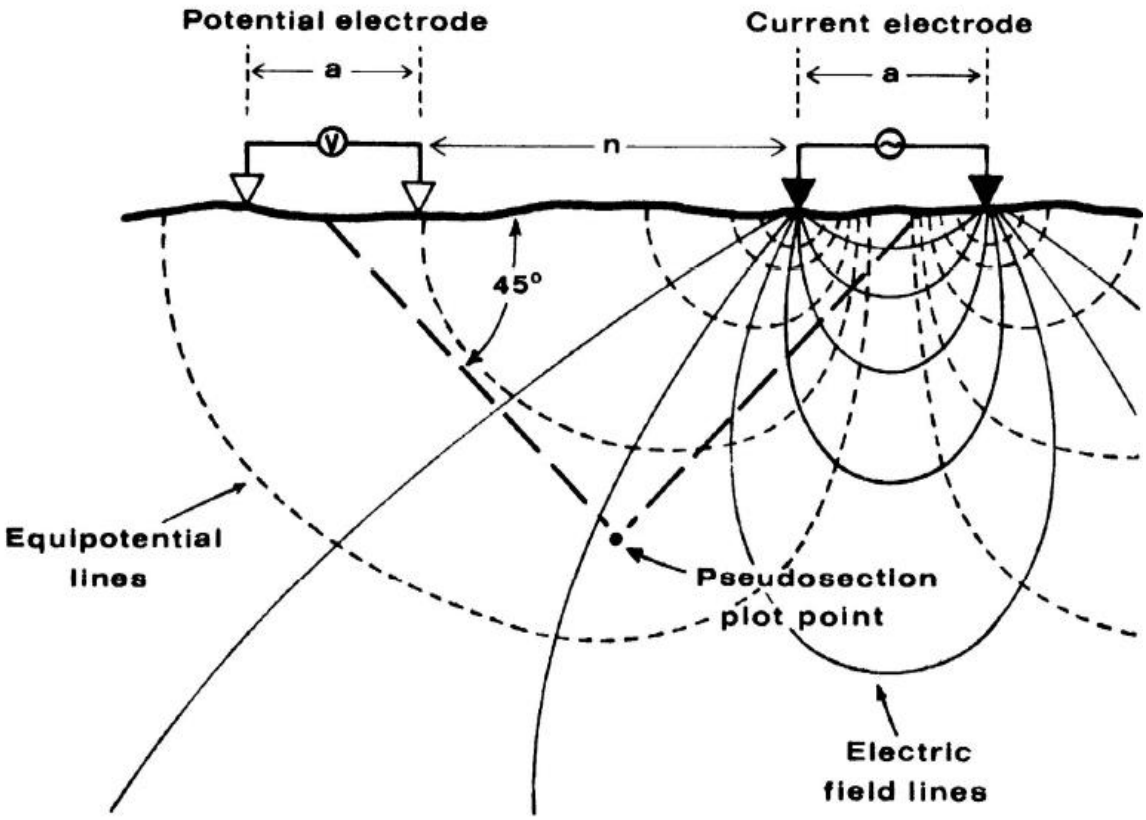

Figure 9: The dipole-dipole array with current flow lines and lines of equal potential. (Ogungbe et al., 2010)

The dipole-dipole array configuration was selected based upon the results of two studies that reveal that this configuration is the best for field investigations because of the high signal to noise ratio and ease of deployment (Sandor and Laszlo, 2008; Stummer, 2004). The dipole-dipole array was deployed in the field with a preset program that created a command file that can be imported into the sting unit in the field. The preset program used multiple command lines that changed the (n) and (a) values (see figure 9) associated with the measured resistivity value (pseudosection plot point). Each of the ER

lines was deployed by driving 42 or 84 stakes and connecting the electrodes (that are built into the ER line) to the driven stakes.

The Electrical Resistivity profiles were processed using inversion programs called EarthImager 2D and EarthImager 3D (www.agiusa.com). In the 2-D EarthImager program, the inversion process uses the average background resistivity as the starting model, which will be discussed below. This program cannot use a user generated forward model as the starting model for the inversion. However, the user can create a forward model and invert it to check for artifacts that the program might generate. Another advantage of the 2-D program is that it quickly produces a 2-D resistivity model.

The 3-D EarthImager has all of the capabilities of the 2-D, but it can model in three dimensions. This capability means that the processing time is significantly longer than the 2-D computation. For comparison, the 2-D inversion takes no more than 1 minute to run but the 3-D inversion can take hours depending upon the settings.

6. Data Processing

6.1 GPR

Processing steps are listed in Table 2 and summarized here. After gathering the GPR profiles, the first processing steps were to apply DC removal and a time-zero correction. The DC removal step is necessary to remove the DC offset that is inherent in the antenna and receiver. If this step is omitted, the traces in the profile will have inaccurate signal amplitudes and therefore will lead to a misleading visual image of the data. Useful signal in each trace was limited to the first 100 nanoseconds because the signal was completely drowned out by noise after 100 ns. Implementing the DC removal requires calculating a mean amplitude value using the first 100 ns of each trace. If values

in the trace differ from the calculated mean, the values were corrected by subtraction of the mean. The mode setting chosen was the mean because it was believed to be the best representation of the average.

The time-zero correction is necessary to compensate for the air/ground boundary time delay of the first arrival. This is an important correction because if the arrival time is inaccurate, the estimation of the associated depth will also be inaccurate (Jol, 2009). Implementation of this process requires the user to enter three parameters. These are first break (visual first arrival), antenna separation (predetermined by the manufacturer) and the velocity of the medium between the antenna and receiver. All processing in this study used a first break of 10.3 ns, an antenna separation of 0.3 m, and a velocity of 14 cm/ns. The velocity value chosen was based upon an average of sand and clay velocities (Reynolds, 2011).

The next processing steps involve application of a background filter and a band pass frequency-wavenumber (F-K) filter. Filtering has to be done to remove signals that have low signal to noise ratios. This is important because if this is not done, then there could be smearing in the boundary locations leading to false interpretation of boundaries.

Table 2: Outline of the GPR processing steps.

Processes	Used	Parameters	Chosen Parameters
Spatial Interpolation	**NO**		
DC Removal	**YES**	**Start time (ns)** **End time (ns)** **Mode** • **Mean** • **Median** • **Alpha trimmed percent**	**0** **100** **Mean**
Trace Edit	**NO**		
Topography	**NO**		
Time-Zero Adjustment	**YES**	**First Break (ns)** **Antenna separation (m)** **Velocity (cm/ns)**	**10.3** **0.3** **14**
Reflection Strength	**NO**		
Bandpass Filtering	**YES**	**Low cut (MHz)** **Low pass (MHz)** **High pass (MHz)** **High cut (MHz)**	**0** **102** **313** **395**
2D Spatial Filtering	**NO**		
Predictive Deconvolution	**NO**		

Amplitude Correction	**YES**	**Automatic Signal Gain (ASG)**
		• **Operator length (ns)**
		• **Type of ASG scalar**
		  ○ **Mean or RMS**
		• **Basis for scalar**
		  ○ **Centered, leading, trailing**
			ASG
			• **100**
			• **Mean**
			• **Leading**

Implementing the background filter requires only one parameter, defining the resolution of the filter. The parameter gives options of weak, normal and strong, which corresponds to a resolution of low, normal and high respectively. The weak background filter creates a large horizontal moving window over the profile, the normal background

filter creates a moving window that is narrower, and a strong background filter uses a moving window made up of a few traces. The filtering removes unwanted signals that are consistent across the entire profile (Jol, 2009). One use for this filter is to remove a signal that is produced when there is an air pocket present between the GPR unit and the subsurface. Despite its usefulness, the background filter could only be used in one GPR profile as discussed below because application distorted portions of the signals of interest.

The bandpass F-K filter (also called an F-X filter) will remove additional noise for each individual trace in the time domain. A bandpass F-K filter that was chosen for the 250 MHz profiles. The signal to noise ratio peaked at 207.5 MHz, so this value was chosen to be the center frequency. The entire frequency band of the profile ranged from 0 MHz to 395 MHz. The bandpass was between 102 MHz and 313 MHz and frequencies on either side were tapered to remove high frequency noise that could be generated near the sharp cutoff bandpass limits (e.g. Gibbs phenomenon) (Hewitt, 1979).

The final steps used were to apply a Stolt F-K migration where needed and an automatic signal gain (ASG) to the profiles. Implementing the F-K migration is useful to correct for dipping layers (Jol, 2009). The only parameter that is needed is to define the migration velocity. This was done using the built-in function in the RadExplorer software that created a hyperbola.

The user can then adjust the hyperbola so that it matches the reflection signatures in the profile. The Stolt F-K migration was only used on one GPR profile as discussed below.

ASG will bring out deeper boundaries and geophysical features. This is done using an automatic gain function that windows each trace. The gain is based upon the difference between the mean amplitude in the windowed signal and the maximum amplitude of the trace (Jol, 2009). This process requires three parameters: operator length for the window, ASG scalar and the basis for the scalar (table 2). The operator length was chosen to be the first 100 ns of the traces. The ASG scalar was chosen to be the mean because it best represents the average of the entire trace. The basis for the scalar was chosen to be the first arrivals of the trace because the signal amplitudes were the largest.

After all of the above processing steps, the 2-D profile was changed from distance vs time to distance vs depth using an average of the velocities of wet sand, dry sand, wet clay, and dry clay for the depth conversion. This resulted in a single overall velocity estimate of 12 cm/ns (Reynolds, 2011). Nevertheless, a value of 14 cm/ns was chosen as being a more realistic estimate given the amount of dry sand at the sites. This chosen value is consistent with the velocity ranges given by Reynolds (2011).

6.2 Electrical Resistivity

The 2-D Electrical Resistivity (ER) surveys were processed through the inversion procedures outlined in Figure 10. The first step was to input each of the measured ER surveys. Each survey was composed of hundreds of individual resistivity measurements at different X (parallel to survey length) and Z (depth) coordinates. EarthImager 2-D calculated an average resistivity value for each 2-D ER survey to create a 2-D starting model for each survey (m_1). The starting model was compared to its corresponding

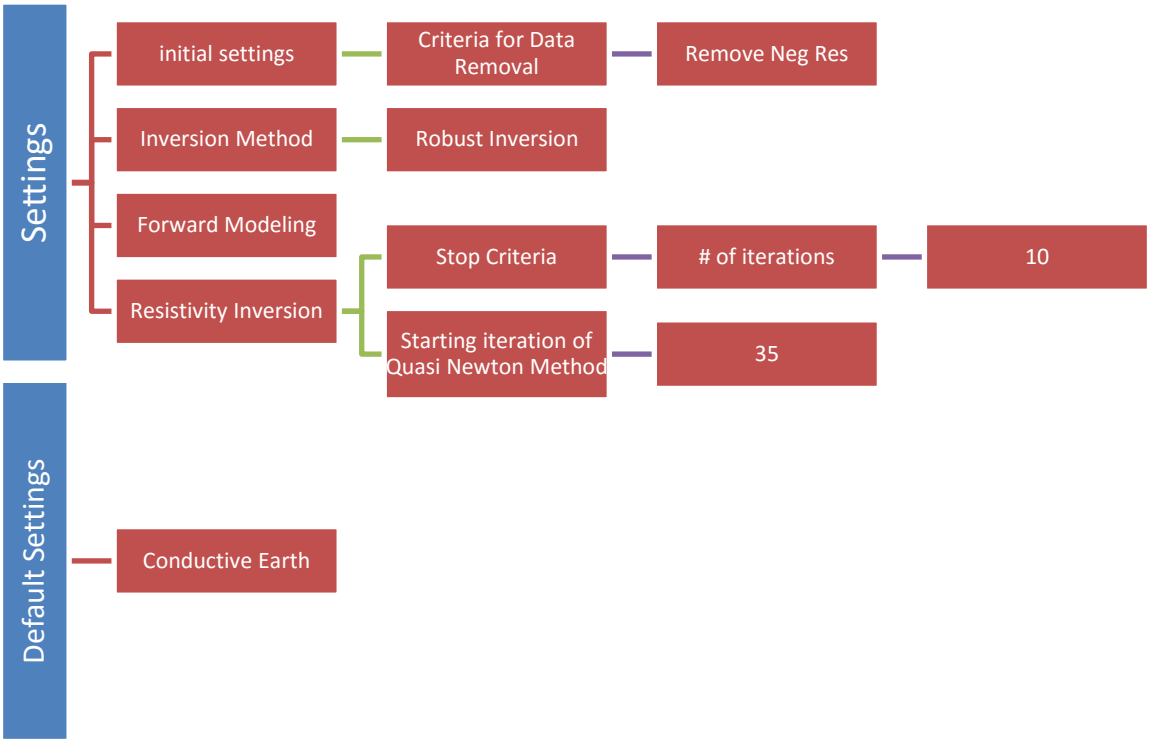

Figure 10: The steps used to process the ER profiles.

measured ER survey and a data misfit between the starting model and the measured survey was calculated. Figure 11 illustrates a typical plot of data misfit for a survey.

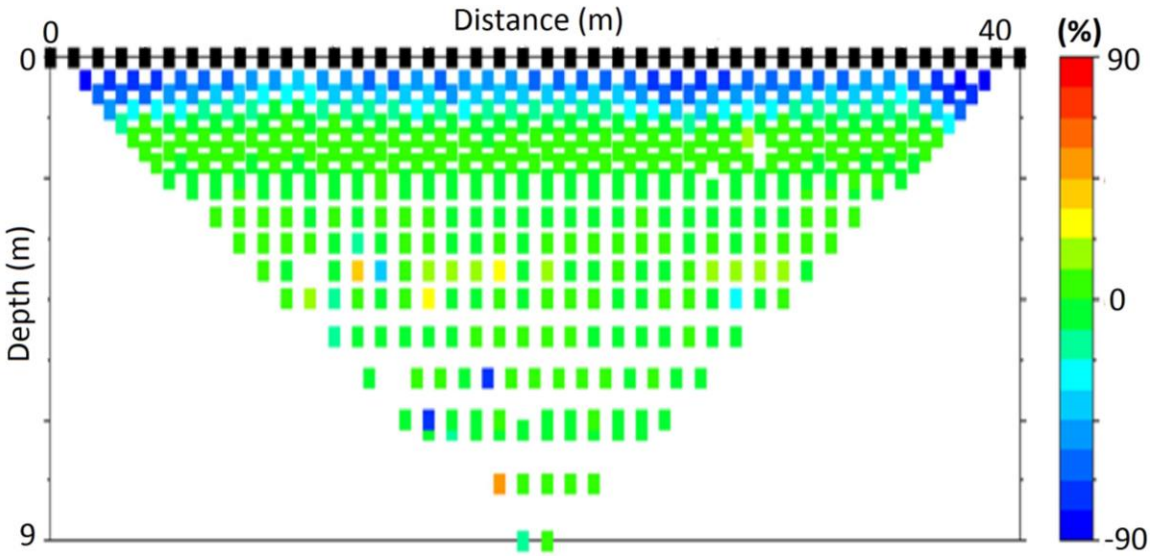

Figure 11: Data misfit scatter plot between a starting model and an ER survey. The data misfit scatter plot was made using data from the eastern-most line at Montrose (site 1) used in the 3-D ER grid.

From this misfit, a normalized root mean squared (RMS) error was calculated which quantified the deviation between the starting model and the measured ER survey. If the RMS error was deemed to be acceptable, the process stopped and the starting model was used as the inversion output. Otherwise, the program solved a linearized inverse problem based upon the starting model and data misfit. The starting model was then updated using: $m_{i+1} = m_1 + \Delta m$, where m_1 is the starting model, Δm is the model update, and m_{i+1} is the new updated model. The program then compared the new updated model to the original measured ER survey and calculated a new data misfit. Likewise, a new RMS error was calculated. If the new RMS error was not acceptable this

process was then repeated until the number of iterations completed was 10 or the RMS error was ≤ 10%. At this point the inversion process created a final updated model that was used as the inversion output. The resulting model was then evaluated by determining its RMS error.

A crossplot of the 2-D survey vs the resulting model was created as a visual representation of the associated RMS error. This revealed how much each individual resistivity measurement in the 2-D survey deviated from the corresponding predicted resistivity value in the resulting model. An example of such a crossplot can be seen in figure 12.

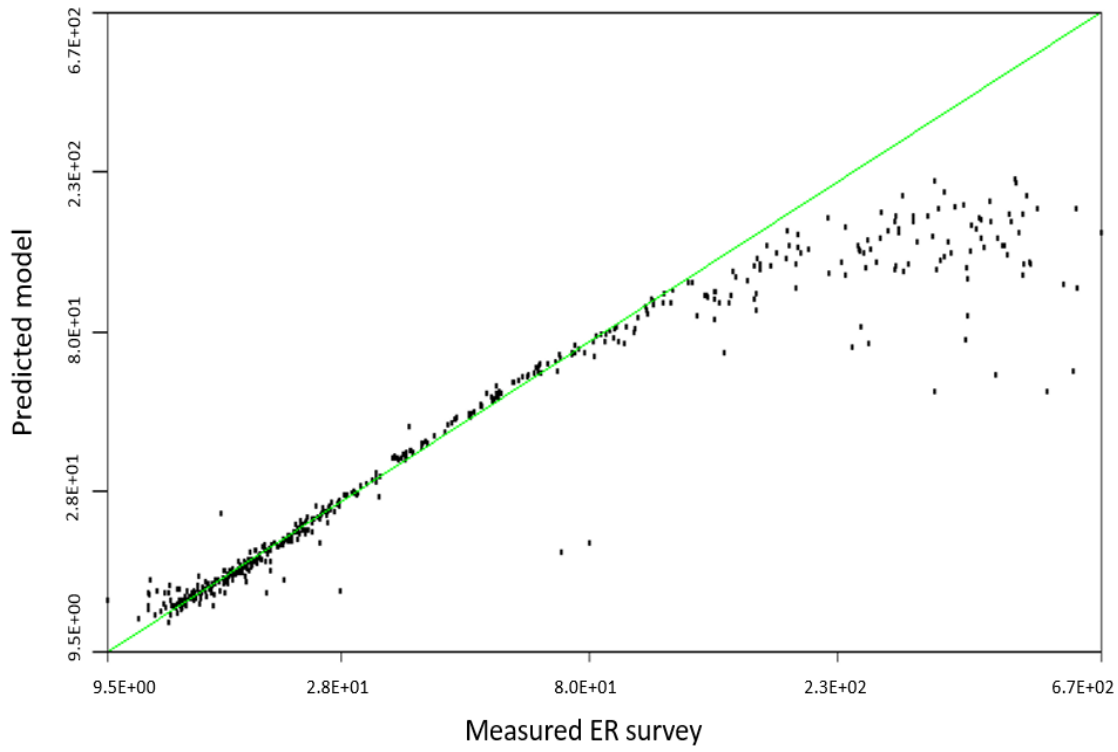

Figure 12: Example of a crossplot of a 2-D survey vs the resulting model. The green line represents a hypothetical perfect fit between the survey and resulting model. The crossplot was made using the same data used in Figure 11.

In order to remove outlying data and improve the overall data fit, a histogram was constructed for each crossplot. An example can be seen in figure 13. The histogram graphically illustrates the data misfit between the resulting model and the corresponding survey. The outlying 10 percent of the crossplot vales were removed.

The inversion process was then repeated with the corrected survey data. This entire procedure (inversion and survey correction) was repeated until the RMS error between the model and corrected survey was reduced to 10 percent or less.

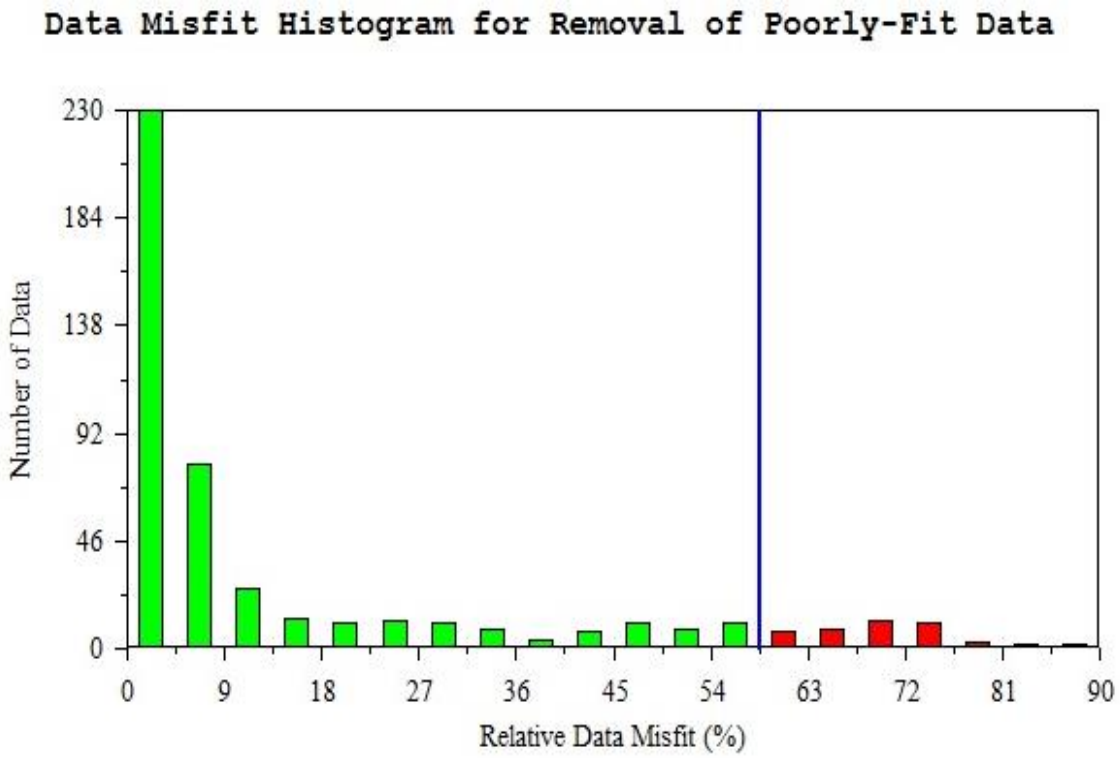

Figure 13: Histogram of data misfit. Blue line divides the outlying 10% of the data, represented by the red histogram boxes. The histogram was made using the same data used in Figure 11.

The initial settings chosen for inversion were the default conductive earth settings. Five alterations were made to these settings. 1) The inversion method was changed from

smooth to robust to reduce the RMS. Selecting the robust inversion method allowed the model to converge quicker by maximizing the reduction of the RMS over each integration. 2) The quasi-Newton value was changed from 20 to 35. The Quasi-Newton value is a smoothing factor, which necessitated increasing the value from 20 to 35, which reduced the impact of the Quasi-Newton method. 3) The maximum number of iterations used as the inversion stopping criteria was changed from 8 to 10, based upon trial and error; 10 iterations maximized the convergence of the inversion model to acceptable RMS values. 4) The RMS error was used rather than the L2 norm (numerical value that quantifies how close the starting model compares to the survey) because L2 was not part of the initial stopping criteria. 5) Removal of negative resistivity values was implemented to constrain the model. The cumulative effect of these five alterations to the initial settings produced a more realistic model.

3-D models were created by using the entire data set, consisting of the multiple 2-D measurement profiles. At site 1, nine 2-D surveys were gathered with an equal spacing of 1 meter apart. Similarly, ten 2-D surveys were collected at site 2. For each location, the entire data set that was collected was used for a complete 3-D inversion. The 3-D inversions were processed in the same way as the 2-D inversions.

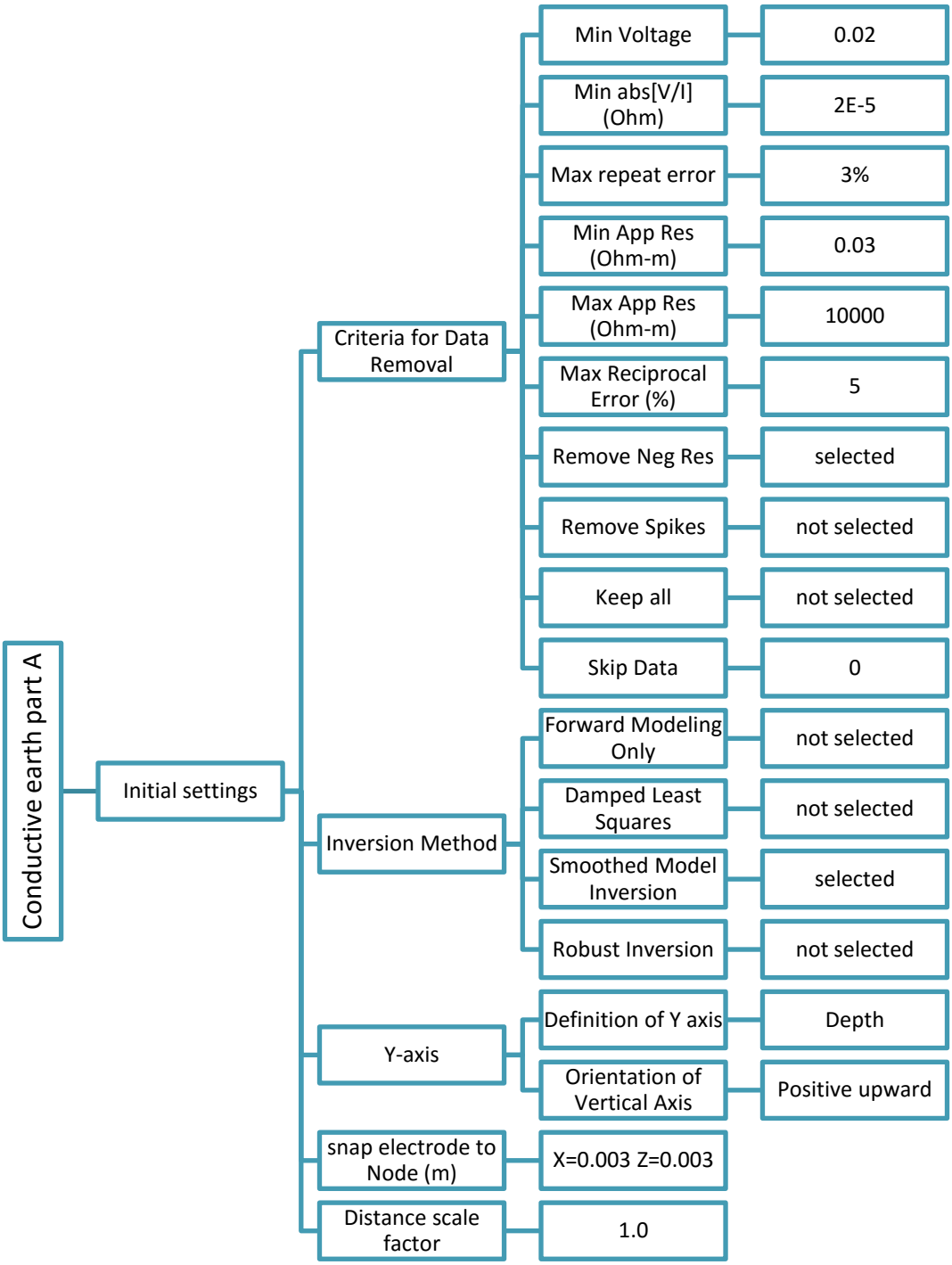

Figure 14: Part A of the default settings for conductive earth.

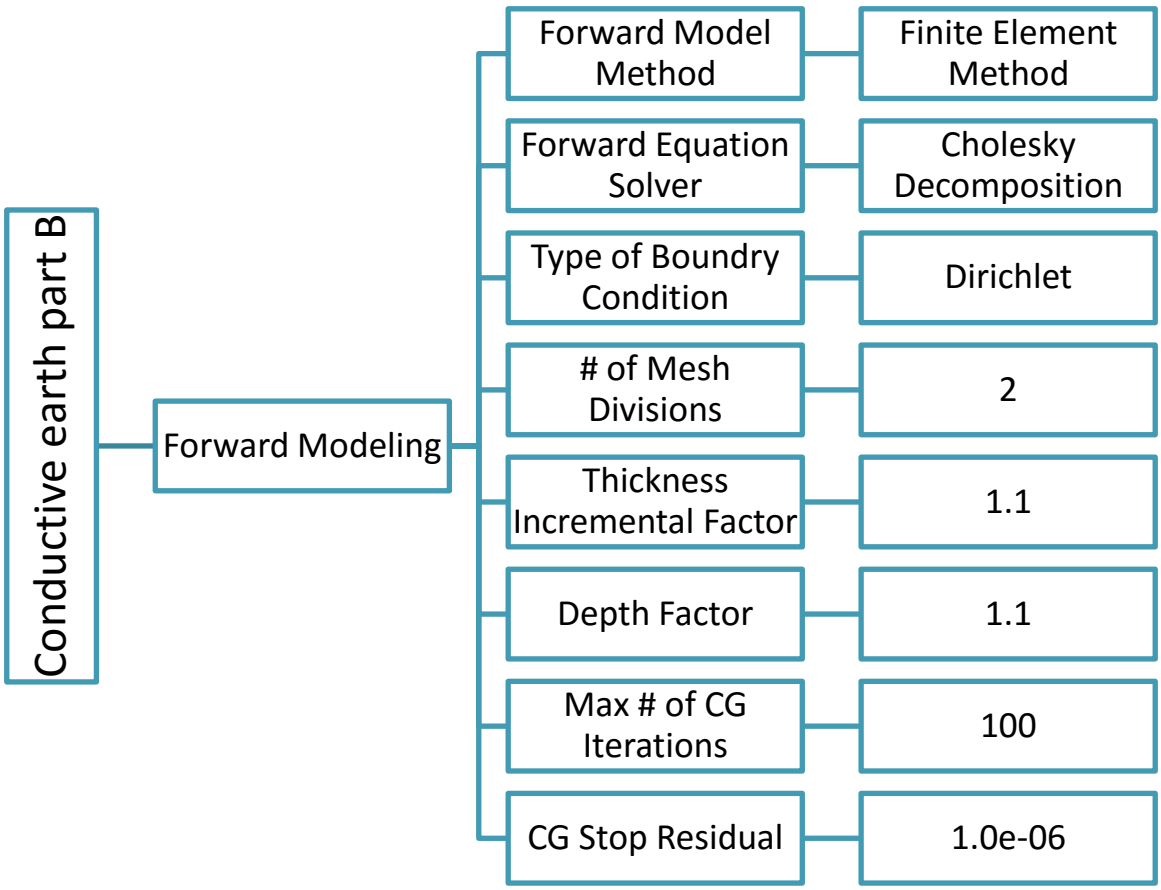

Figure 15: Part B of the default settings for conductive earth.

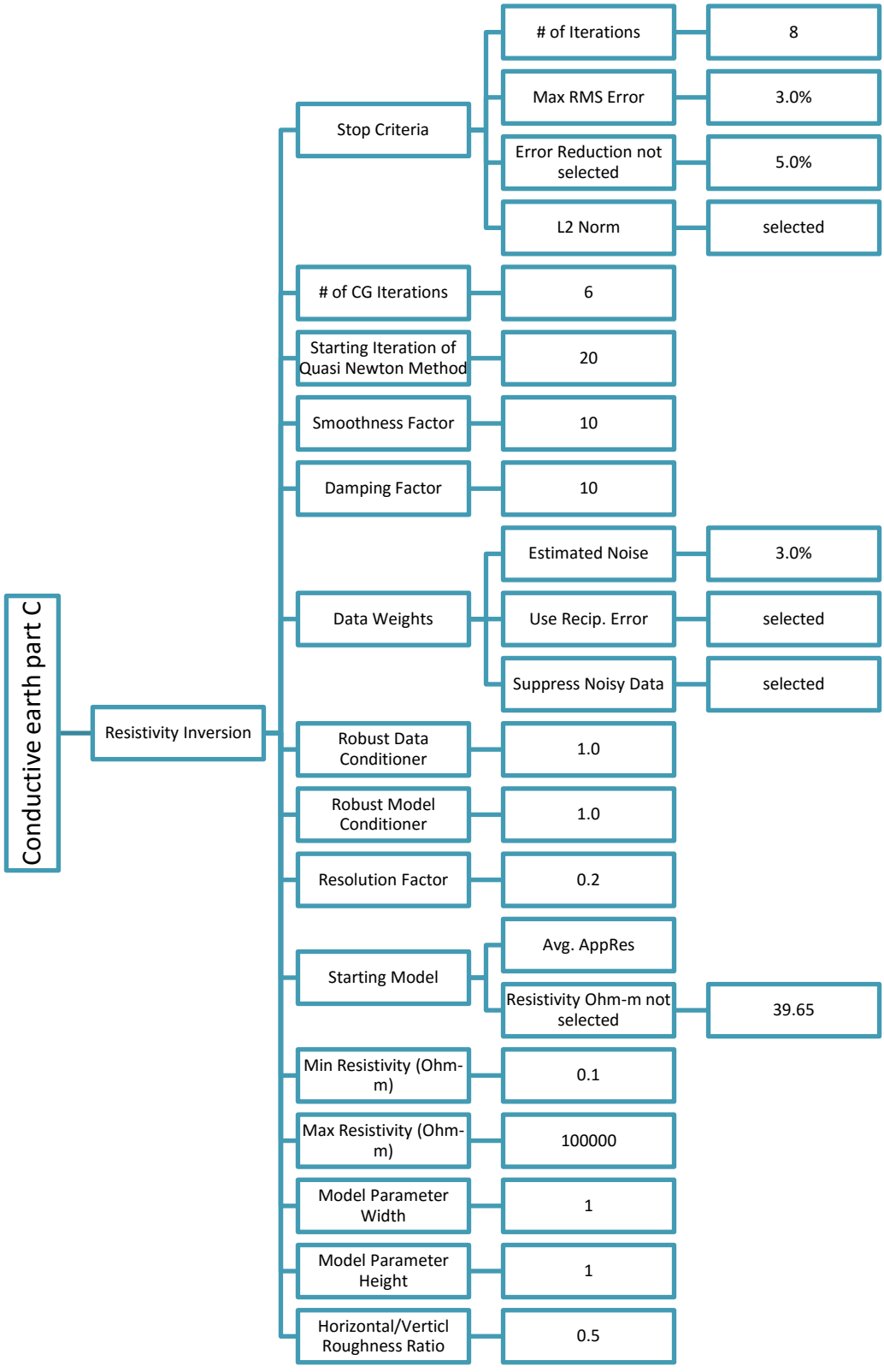

Figure 16: Part C of the default settings for conductive earth.

6.3 Synthetic Model

Once the processing parameters were chosen, a simple 2-D forward model was created to test the inversion procedure (figure 17). For simplicity, the model consisted of only three different earth materials; dry sand, clay and groundwater. Based upon borehole studies, the two most common earth materials in the near surface geology were sand and clay (Cox et al., 2007). Each of these materials has a distinctly different electrical resistance. Average resistance values were chosen, i.e. 565 Ohm-m for sand and 100 Ohm-m for clay. Groundwater was assumed to be similar in composition to rainfall runoff and thus assigned a value of 60 Ohm-m (Reynolds, 2011).

The forward model consists of three highly resistive dike-like structures (sand dikes). The surrounding stratigraphy consists of alternating high and low resistive layers (sand and clay). The alternating layers reach a depth of about three meters, the estimated depth of the water table (Randy Cox personal communication).

Once the forward model was created it was inverted with the same parameters that were used for the surveys. The sand dikes were recovered but possible smoothing effects affected the model below three meters, producing the circular-like structures in the center of a low resistivity region.

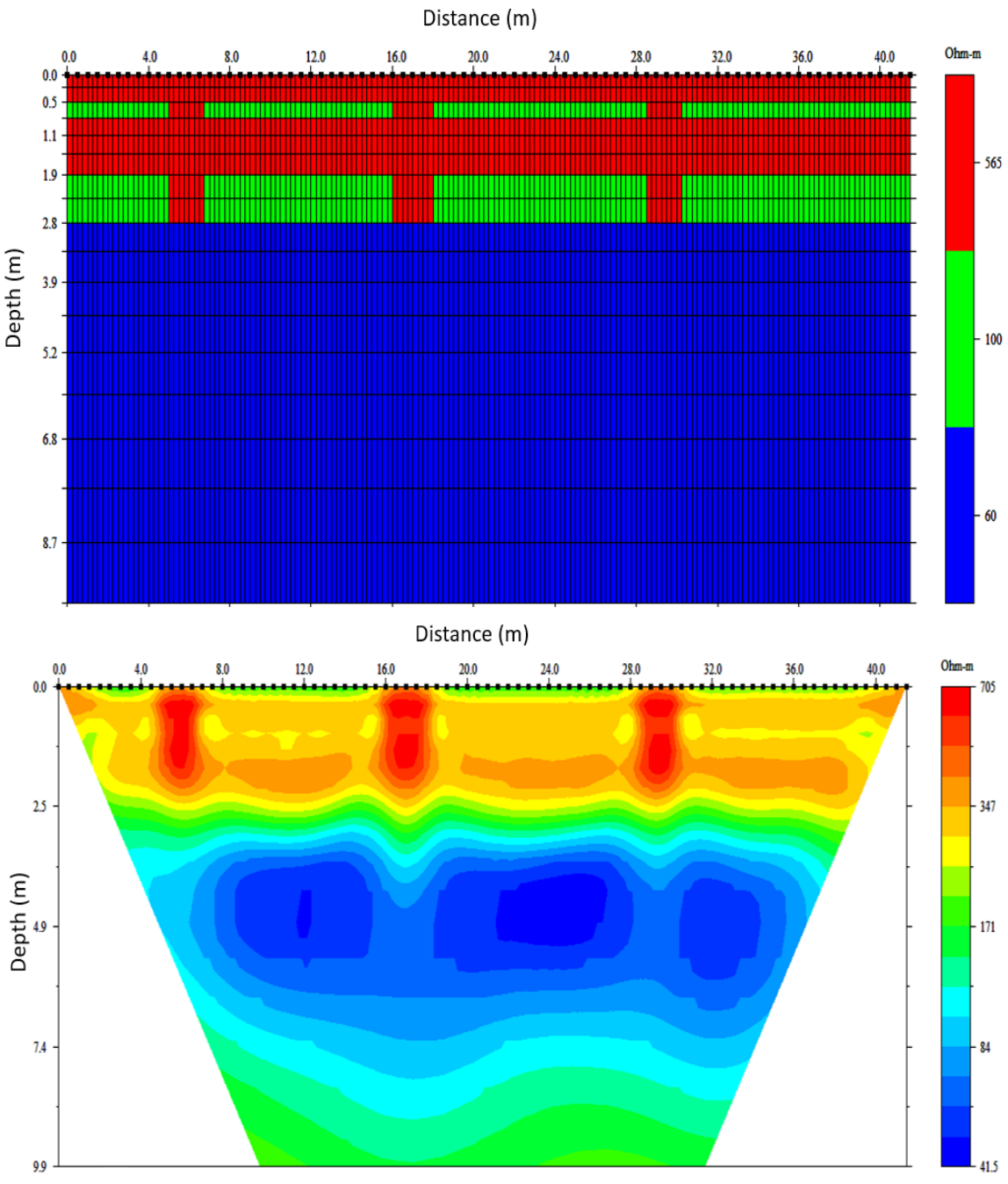

Figure 17 Shows the forward model (top) and inversion model (bottom) that simulates highly resistive structure that mimic sand dikes. Note, the resistivity color scale of the forward model and that of the inversion model are not the same

7. **Results**

7.1 Morgan Site

The results at the Morgan site involve nine GPR surveys. However, three GPR surveys are shown because they are the best of the nine taken in the 3-D grid area (figure 5). The first (eastern-most) GPR profile is made up of 780 traces that extend to a depth of 4.0 meters (figure 18). The length of the entire profile is 40 meters. The profile shows alternating layers of sand and clay that extend across the entire length of the profile and reach a depth of 2.5 meters. Between the depths of 0.5 to 2.5 meters the alternating layers of sand and clay are not uniformly striated across the profile, but instead show many angular unconformities and alternate dipping up and down. Below 3.0 meters the signal to noise ratio is very low and the signal is lost.

The associated ER model has resistivity values between 1.8 and 176.0 Ohm-m. The model has two regions of high resistivity located in the depth ranges 0.0 and 2.5 meters and 6.0 to 9.9 meters. The highly resistive region near the surface has multiple elliptical anomalies indicating the locations of highly resistive material. These ER anomalies are spatially correlated to zones of disrupted GPR reflectors. Between the depths of 2.5 and 6.0 meters the model has a low resistivity layer with similar elliptical anomalies but, in this case, depicting areas of very low resistivity.

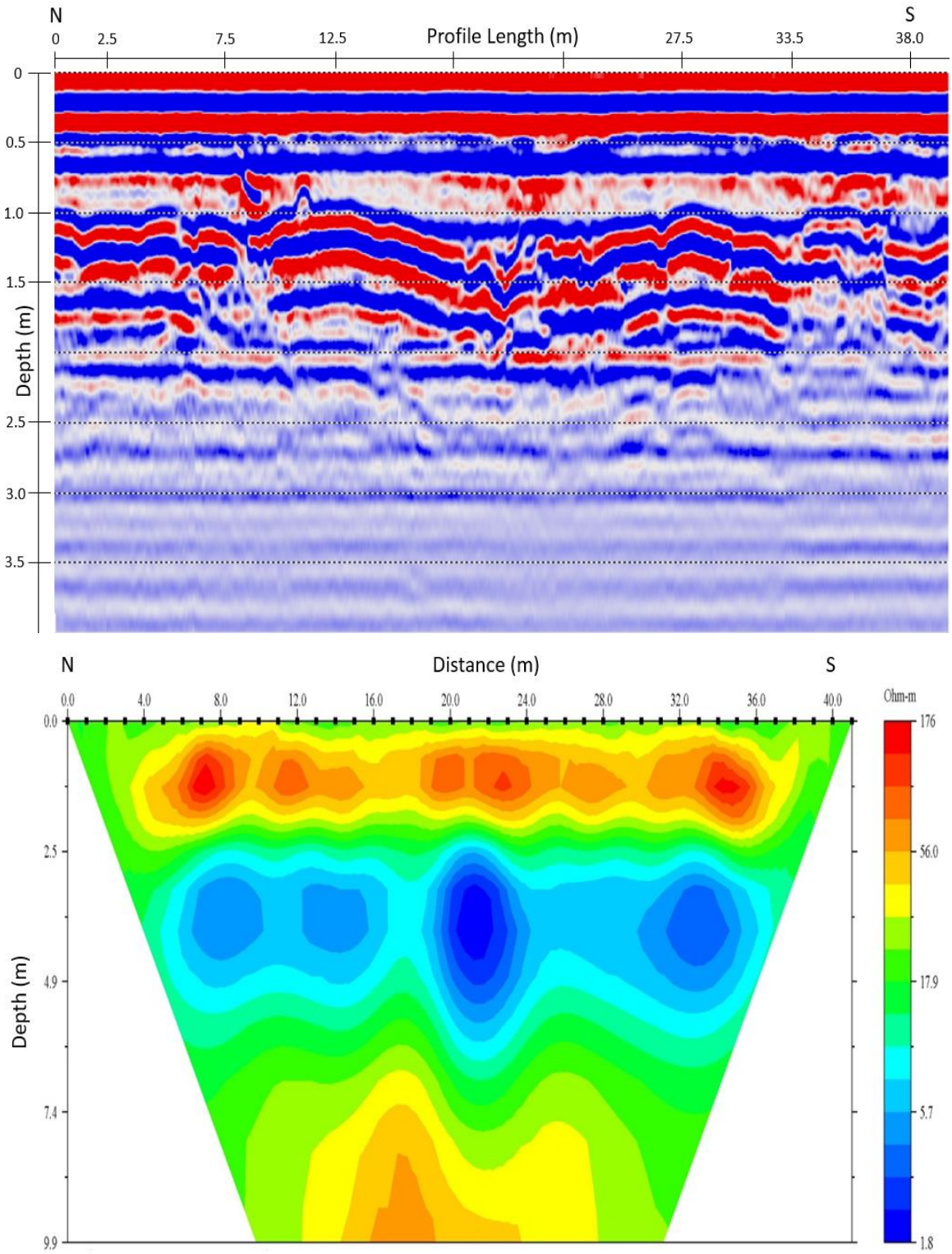

Figure 18: The eastern-most line at Montrose (site 1) used in the 3-D ER grid. Top: the GPR profile. Bottom: the corresponding ER model with a RMS of 9.11%

The second (western-most) GPR profile is made up of 780 traces that extend to a depth of 6.0 meters. The length of the entire profile is 41 meters. The profile shows alternating layers of sand and clay that stretch across the entire profile (figure 19). However, between the depths of 0.5 and 3.5 meters the alternating layers of sand and clay are not uniformly striated, similar to the easternmost profile. Below 3.5 meters the signal to noise ratio is very low and the signal is lost.

The corresponding ER profile has two regions of high resistivity between 0.0 and 2.5 meters depth and between 6.0 meters and 9.9 meters depth. The highly resistive region at the surface has multiple elliptical anomalies that indicate the presence of highly resistive material, similar to the easternmost profile. The middle depth portion of the model has a low resistivity layer with elliptical shapes indicating regions of very low resistivity.

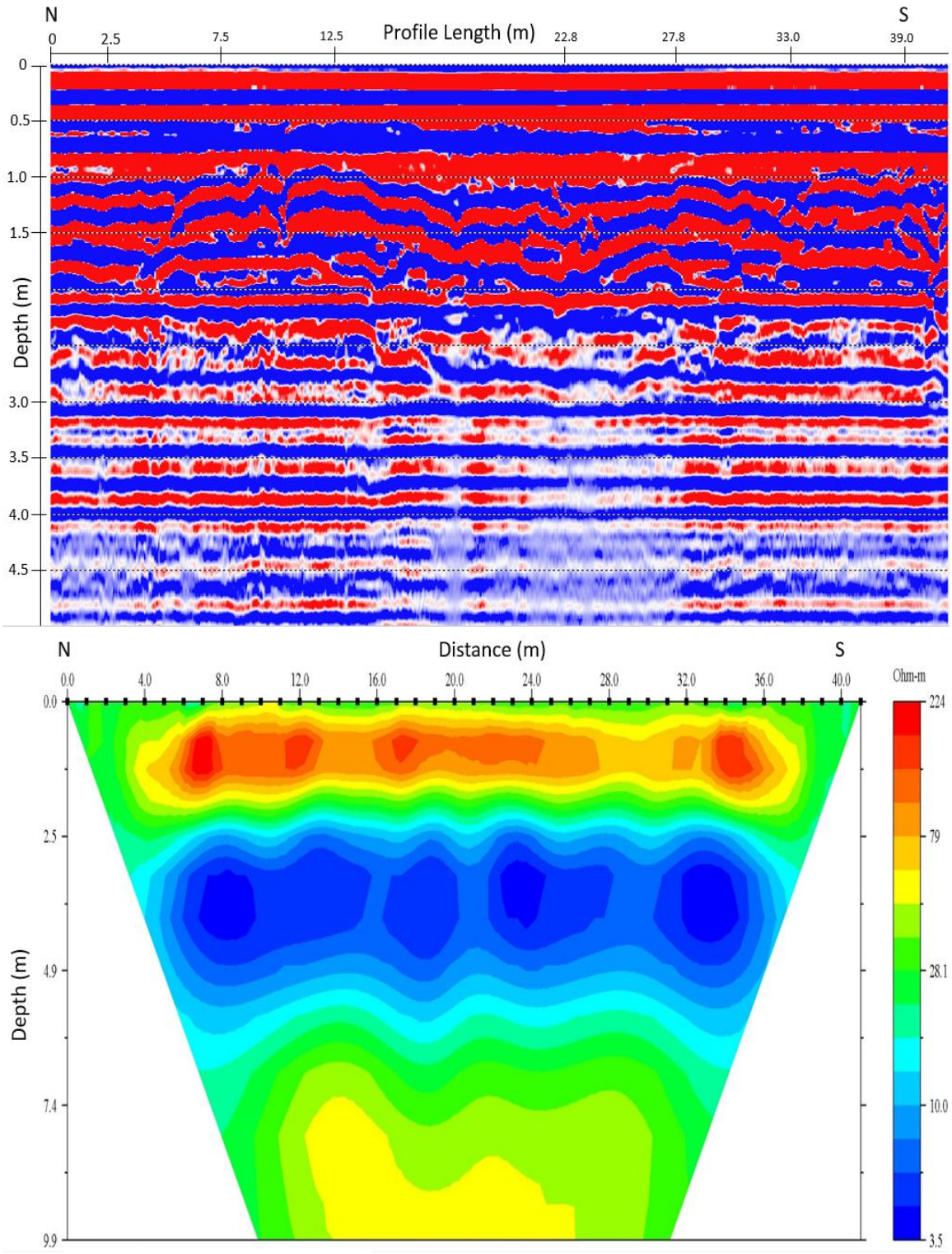

Figure 19: Same as Figure 18 but showing the western-most ER line used in the 3-D grid. The ER model has an RMS of 9.67%

The third (center) GPR profile is made up of 780 traces that extend to a depth of 5.0 meters (Figure 20). The length of the entire profile is 41 meters. The profile shows alternating layers of clay and sand that stretch across the entire profile. The alternating layers reach a depth of 3.0 meters. Between the depths of 0.5 to 3.0 meters the alternating layers of sand and clay are not uniformly striated, like the other profiles. Below 3.0 meters the signal to noise ratio is very low and the signal is lost.

The corresponding ER model has two regions of high resistivity between 0.0 and 2.5 meters depth and 6.0 meters and 9.9 meters depth. The highly resistive region at the surface has multiple elliptical anomalies of high resistivity, like the other profiles. These ER anomalies are spatially correlated to zones of disrupted GPR reflectors. The middle depth range of the model has a low resistivity layer with the same elliptical shapes indicating resistivity lows as seen in the previous profiles.

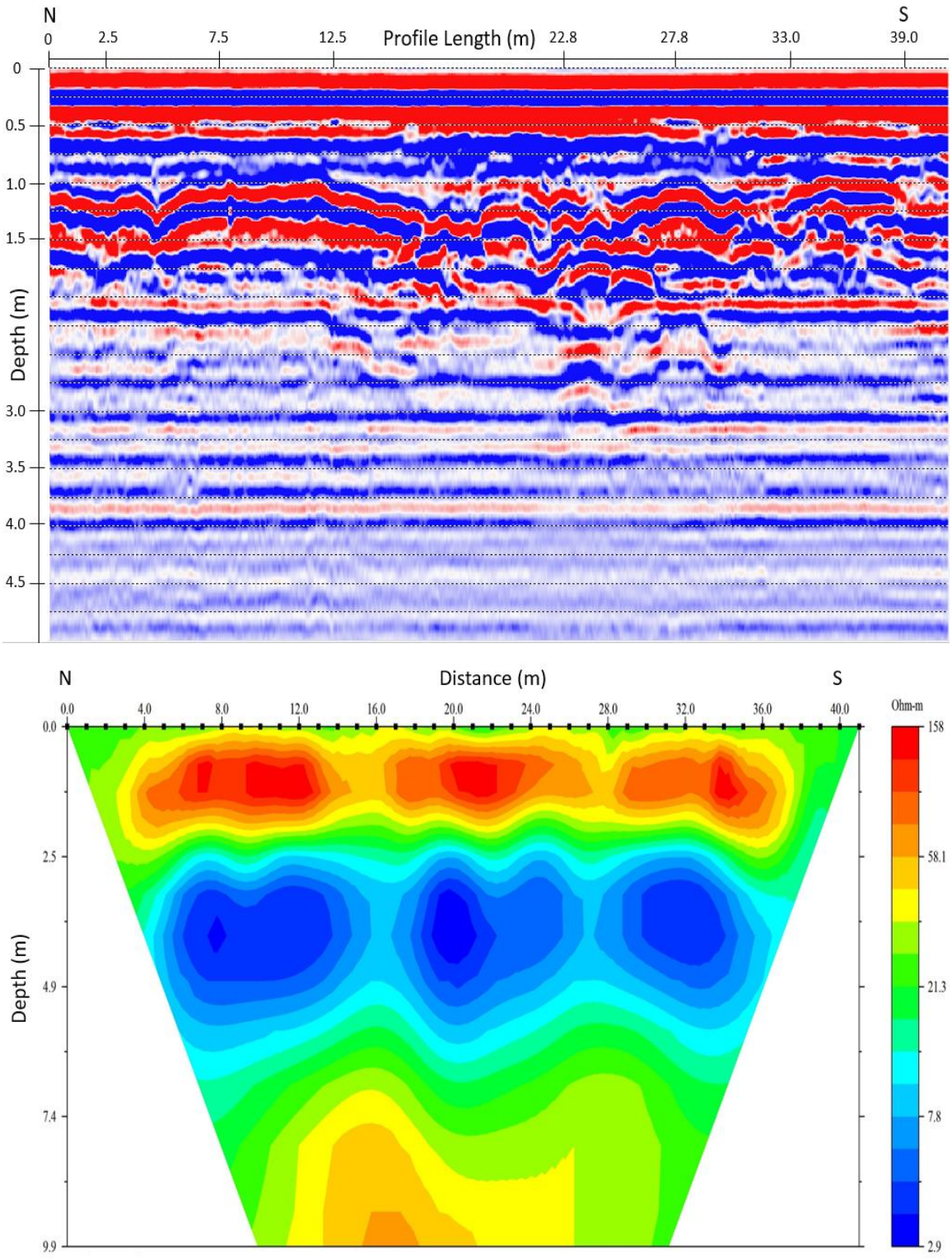

Figure 20: Same as Figure 18 but the middle line used in the 3-D ER grid. The ER model has an RMS of 9.48%

The 3-D ER model is presented in Figure 21 and shows the highly resistive areas that start at around 200 Ohm-m. The model shows elliptical anomalies of high resistivity, similar to the 2-D models. The model is scaled to emphasize regions of high resistivity. Concentrated volumes of high resistivity shown in the figure are numbered and centered at (32, 1, -1.25), (27, 8, -1.25), (21, 1, -1.25), (15, 1, -1.25), (13, 2,-1.25), (8, 8, -1.25) in X, Y, Z format.

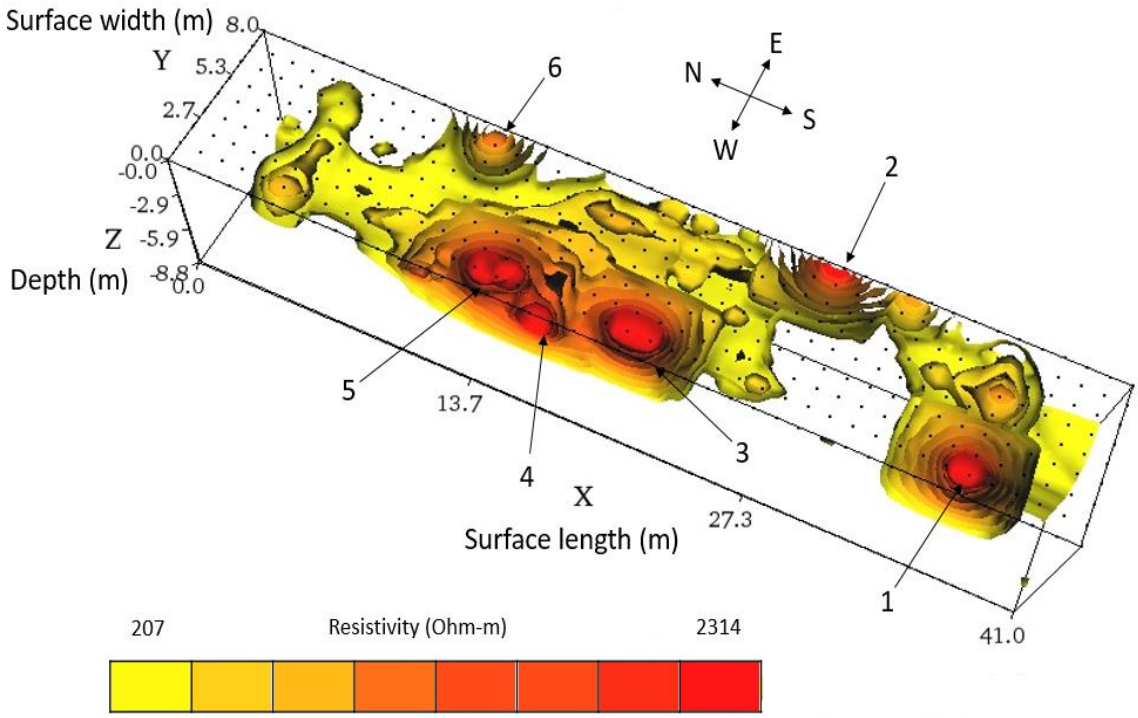

Figure 21: The 3-D inverted resistivity model based upon data collected along the nine 42 meter long resistivity profiles shown in Figure 5. The model has a RMS of 10%. Figure is made to show the top 2 meters of high resistivity.

7.2 Phenix Site

Results at the Phenix site are illustrated using one selected GPR survey (all 10 surveys were essentially identical) and its corresponding inverted ER model, along with the 3-D ER inverted model. The GPR profile (Figure 22) reaches to a depth of 4.5 meters and is 42 meters long. There is a strong signal from 0 to 1 meters in depth. However, below 1 meter the signal to noise ratio is very low and the signal cannot be separated from the background noise.

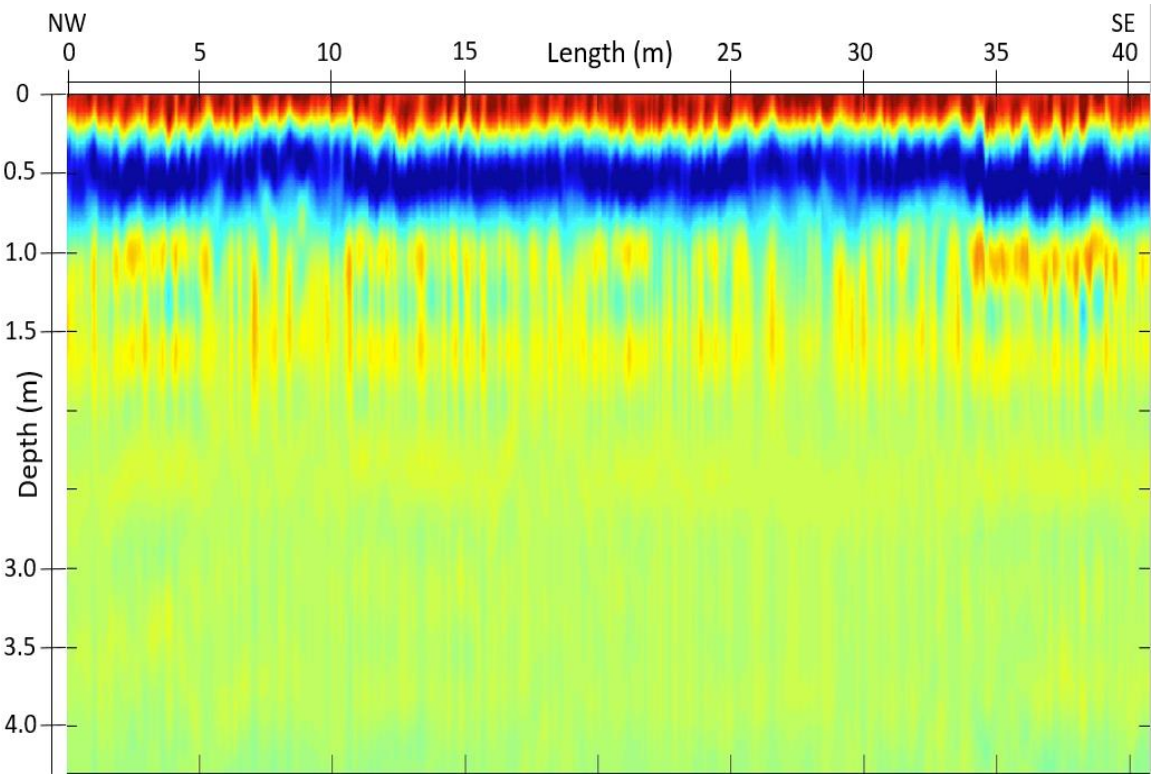

Figure 22: Shows a GPR profile of the Phenix site with a simple depth conversion and normal move out.

The inverted 2-D ER model (Figure 23) shows two distinctive regions, one of high and one of low resistivity. The high resistivity region is between 0 and 2.5 meters deep. Below 2.5 meters there is a low resistivity region that extends to 9.9 meters deep.

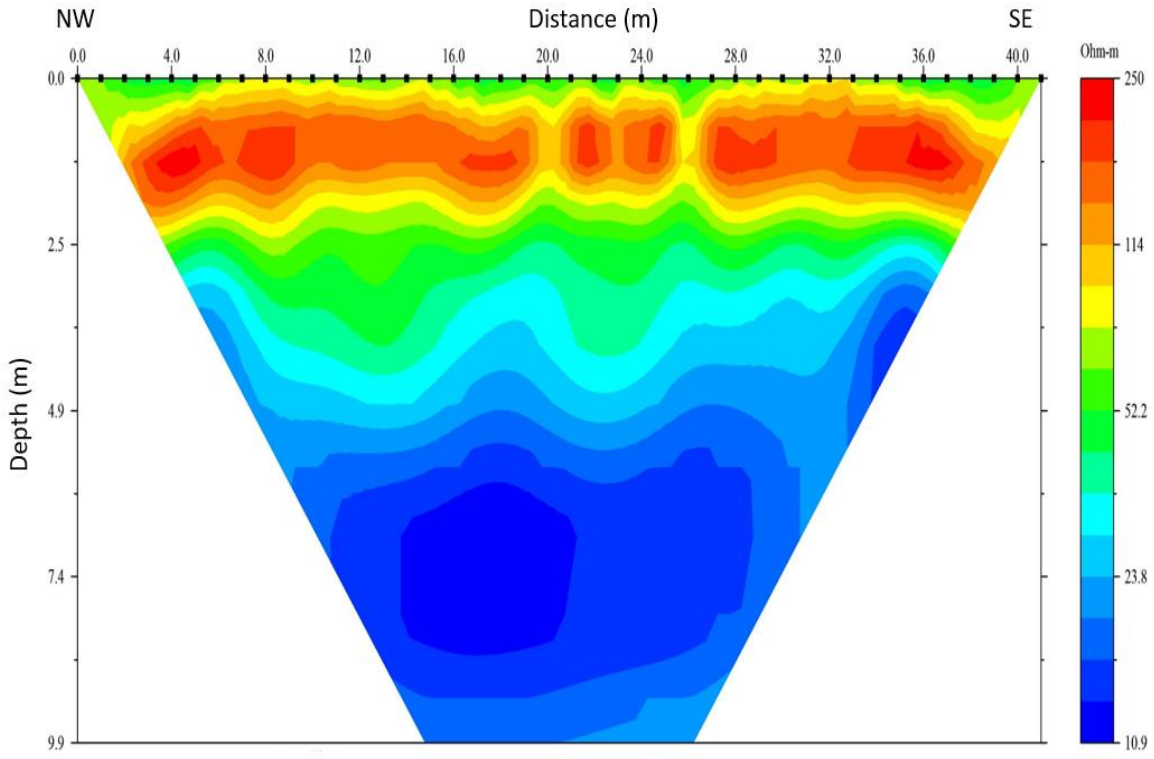

Figure 23: Shows the corresponding inverted resistivity model of the Phenix site (site 2) with a RMS of 5.3%

The 3-D model (Figure 24) only shows the contours of high resistivity that are over 80 Ohm-m. The model shows somewhat elliptical shapes that are highly resistive. These are centered at (30.5, 5.5, -1.5), (25.0, 0.0, -1.5) and (22.0, 0.0, -1.5).

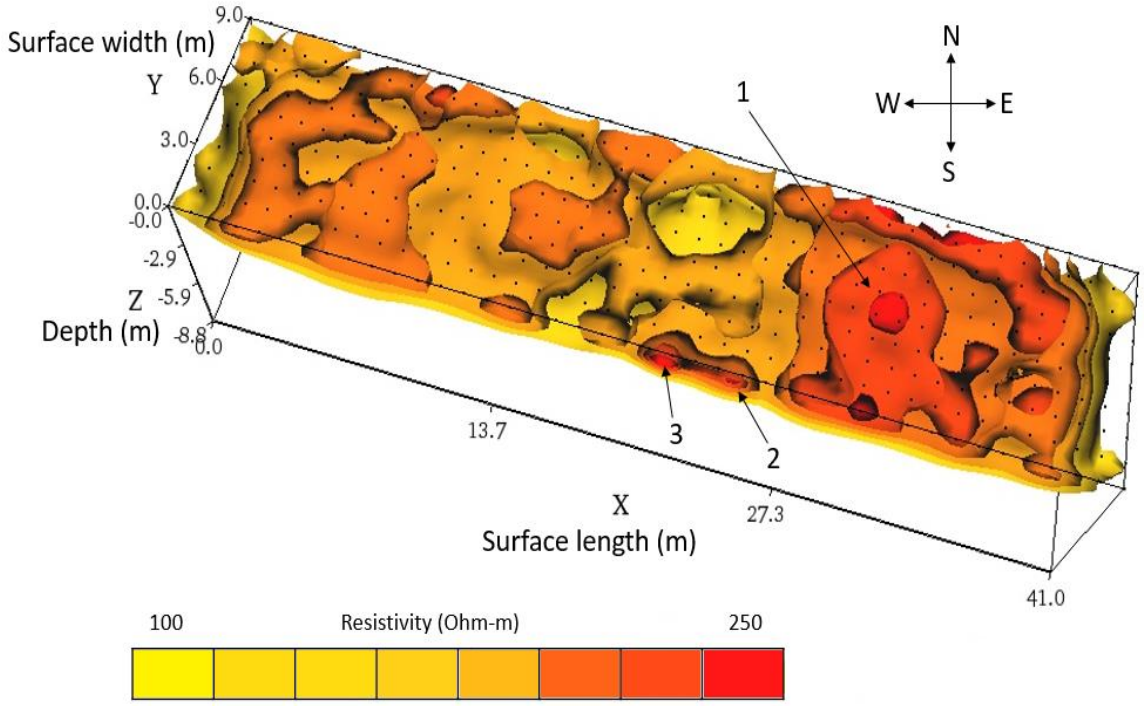

Figure 24: Shows the 3-D inverted resistivity model of site 2. The figure is made to show the top 2 meters of high resistivity with a RMS of 4.6%.

7.3 Morgan Site B

Four GPR profiles were collected at Morgan site B; two using the 100 MHz antenna and two using the 250 MHz antenna. The profiles using the 100 MHz antenna did not reveal any structure. However, one profile using the 250 MHz antenna did reveal a possible structure. A 40 meter section of this profile (Figure 8) is shown in figures 25 and 26. The section has been processed using a background filter on the normal setting and includes about 780 traces. The layers are horizontal but slightly wavy. There are multilayered crisscrossing hyperbolas near the center of the profile shown in figure 25. The profile has a low signal to noise ratio after approximately 100 ns. As the GPR cart was wheeled over that section of the profile, the antenna naturally bounced because of the

patches of grass along the profile. This bouncing created sections in the profile, as shown in figure 25 at meter marker 351, that look like shocks in the data.

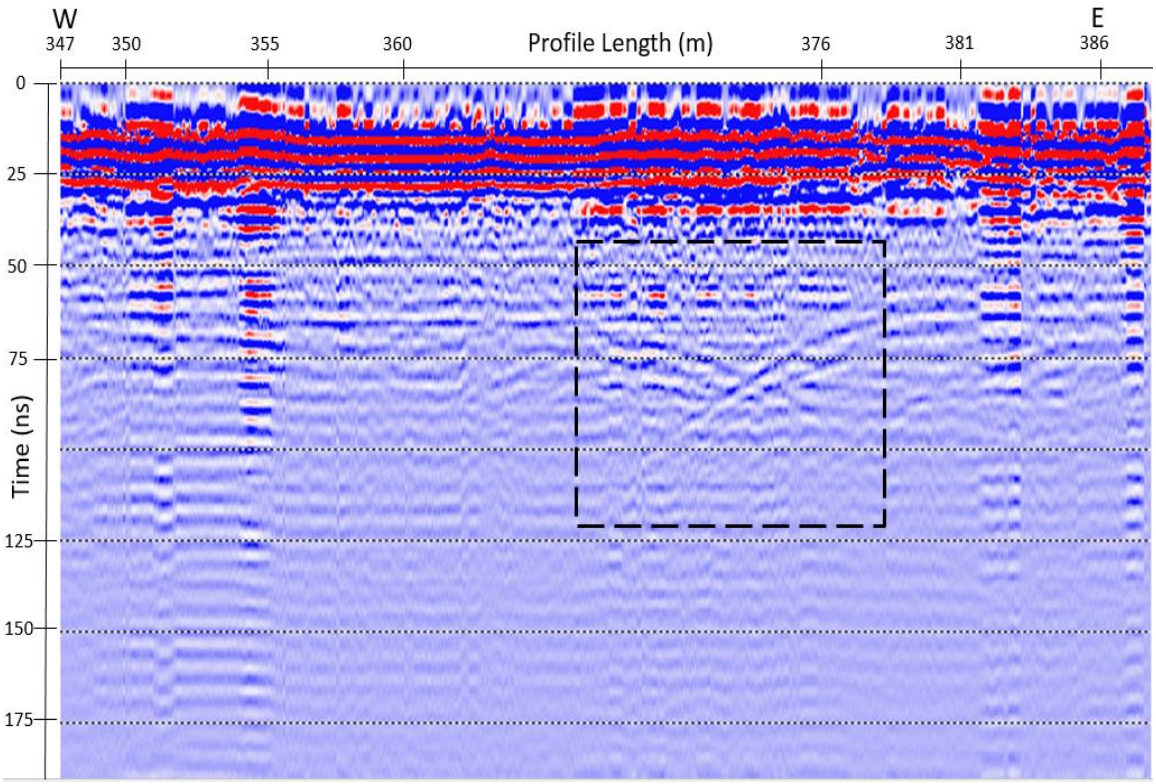

Figure 25: Part of the GPR profile of line 1 using the 250 MHz antenna. This profile has not been migrated. Crossing hyperbolas (bow-tie structure) suggest that there is a synclinal structure present between 363 meters and 378 meters, enclosed in the dashed black box.

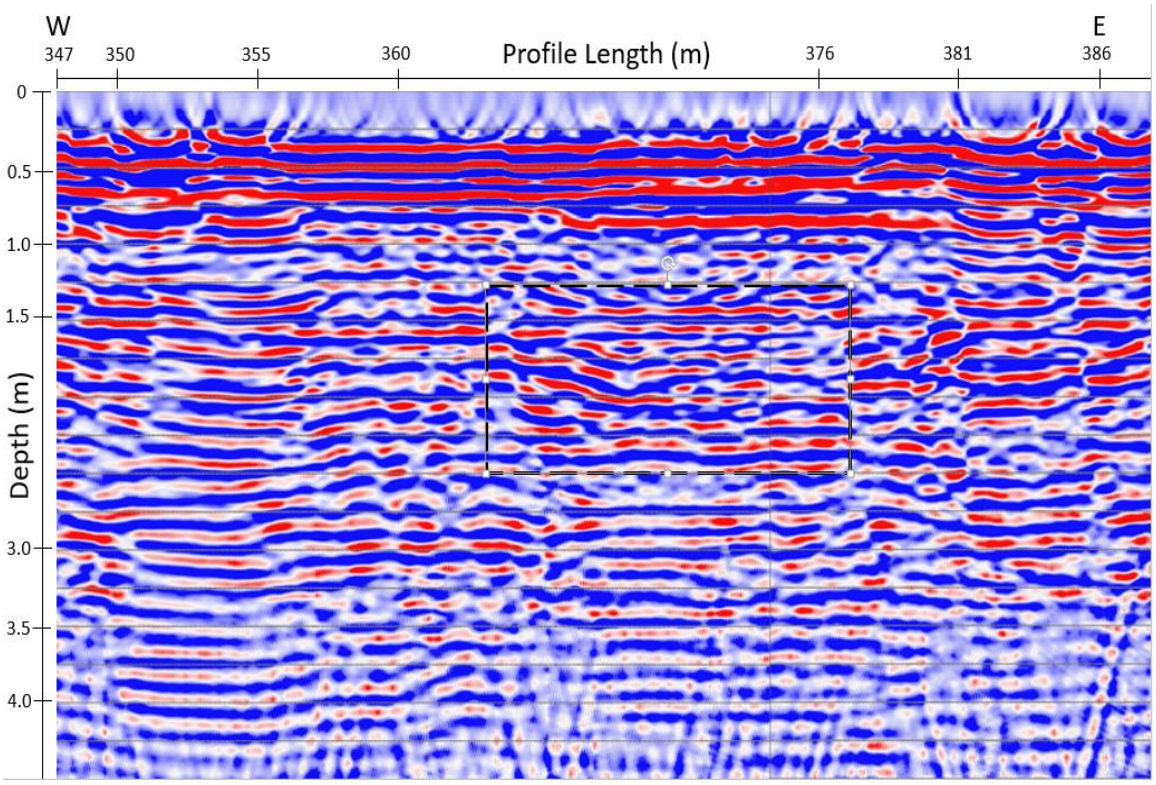

Figure 26: The same GPR profile after migration and depth conversion. The black box encloses the syncline structure.

Figure 26 is the same 400 meter section after implementing a Stolt F-K migration using a velocity of 11.6 cm/ns. The section shows horizontal but slightly wavy layers. One can see a synclinal structure enclosed in the dashed black box that is coincident with the bow-tie structure in the unmigrated section. The section has also been processed using a background filter on the normal setting as in figure 25. The grassy bumps are producing the signals that penetrate throughout the section.

8. **Interpretation**

8.1 Morgan Site

The results at the Morgan site show evidence of multiple sand blows. This is exemplified in all of the figures at site 1. The GPR profile in figure 18 shows three structures at the 7, 21 and 34 meter marks. The structure at meter marker 21 is accompanied by dipping beds, which according to Al-Shukri et al. (2005) is powerful evidence of a sand dike. The other two structures do show dipping beds but they are not as prominent as the structure at meter marker 21. When compared to the resistivity model along the same line, these structures are all highly resistive, which further suggests that these are sand dikes.

The GPR profile in figure 19 shows multiple structures. One such structure, between meter markers 16 and 24, has dipping beds on both sides. When compared to the corresponding resistivity model this structure is highly resistive. Thus, the structure can reasonably be interpreted as a sand dike. There are other structures shown in the GPR profile such as those at meter markers 7 and 34, but the dipping layers are not present with certainty. However, there are two areas in the resistivity model centered on meter markers 7 and 34 that are highly resistive. This leads to the interpretation that these structures are indeed sand dikes.

The GPR profile in figure 20 shows multiple structures, with the most prominent one located between the 16 and 25 meter markers. Like the previous profiles, there are dipping beds on both sides of the discontinuity, which suggest the presence of a sand dike. The corresponding resistivity model also has high values centered at meter marker 21. The other structures at meter markers 10 and 34 shown in the GPR profile show

dipping beds, but these are not as clear. Nevertheless, the resistivity model supports the interpretation that these are sand dikes as well.

Each of the resistivity models reveals elliptical areas of high resistivity. Every one of these elliptical shapes are influenced by the inversion process. They are not artifacts but they have been distorted by the shaping/contouring that takes place in the inversion due to smoothing. These highly resistive elliptical structures have been smoothed more than the synthetic highly resistive dikes in figure 17. Since the real ER survey has less of a sharp resistivity contrast, smoothing has more of an effect.

Alternatively, the low resistivity, elliptical regions below each of the high resistivity regions are probably purely artifacts. Similar elliptical regions were found in the inversion results for the synthetic model shown in figure 17. The figure shows artifacts in the low resistivity region that are similar to those found for the real inverted ER surveys. This low resistivity region almost certainly corresponds to the zone of saturation below the water table. This is further supported by the fact that all of the GPR profiles at the Morgan site have a very low signal to noise ratio below a depth of 3.0 meters.

Overall the Morgan site was a good location at which to image sand blows using GPR and ER. Both GPR profiles and ER surveys contained signatures which was interpreted to be a sand dikes. Just like in the 2-D inverted models, the 3-D inversion model was able to divulge these same signatures, but at a higher resolution.

8.2 Phenix Site

The Phenix site was a relatively poor location to detect sand blows for two reasons. A recent storm produced 2 inches of rain over the study site and the study area

was leveled for agricultural purposes. Under these site conditions the GPR profiles collected had a very low signal to noise ratio, as indicated in figure 22. Further processing was attempted such as F-K filtering, deconvolution and automatic signal gain, but the signal to noise ratio was not high enough for the processing techniques to be effective.

The ER profiles reveal some structures that have high levels of resistivity. However, as shown in figure 23, the areas that have high levels of resistivity are not as clear as those observed at the Morgan site. The 3-D inversion model, figure 24, shows three volumes of high resistivity at the Phenix site that display the same signature as the Morgan site sand dikes that are centered at (5.5, 30.5, 1.5), (0.0, 22.0, 1.5) and (0.0, 25.0, 1.5).

When looking at figure 24, it is apparent that the 2 inches of rainfall played a huge part in the poor resolution of the data because the resistivity range for the inverted 3-D model was reduced by nearly a factor of ten relative to the Morgan site. Despite the poor site conditions, the 3-D model does indicate the possible presence of sand dikes and provides targets for future work.

8.3 Morgan Site B

A possible a fault-like structure has been resolved in the migrated section shown in Figure 26. The feature starts at the 365 meter marker at a depth of 2 meters and extends to the 379 meter marker. This structure is not that clear because of poor site conditions introduced by the rough surface over which the GPR data were collected. This bouncing created noise in the sections that extends vertically throughout the image. Since

this noise is prevalent in the unmigrated section, and more specifically where the bow-tie structure is located, the migrated section is also noisy.

9. Discussion

The ER results from the Morgan site and the Phenix site justify future research in the Mississippi Embayment for finding sand blows using this technique. The 3-D models in Figures 21 and 24 reveal clear signatures of high resistivity that are excellent candidates for sand blow dikes. The minimum width of a sand dike that could be detected with certainty would likely be in the range of two meters. Referring back to figure 18 from the Morgan site, one can see that the sand dike's indicative features might not be apparent if its width falls below this size. Under optimal field conditions, GPR can be used to detect sand blow features. This is illustrated in figures 18-20 for the Morgan site. A clear correspondence between dipping layers in the GPR profiles and regions of high resistivity in the ER profiles was observed. Neither method was able to detect features below the water table. Figures 21 and 24 illustrate the benefits of computing a full 3-D inversion of the ER data; the areal extent of several possible sand blows is clearly indicated in the 3-D images and the results will provide excellent starting models for future trenching investigations.

When field conditions are influenced by recent rainfall, as in the case of the Phenix site, ER profiles may be able to locate sand blow dikes but GPR will probably not be effective. Imaging subsurface features is possible using GPR, depending upon the depth of the feature and the depth of the zone of saturation. A high frequency antenna is optimal for detecting sand blow features. Al-Shukri et al. (2005) obtained excellent results using a 400 MHz antenna. For deeper features such as faults located above the

zone of saturation, detection may be possible using an antenna that has a frequency of 250 MHz or higher. Using the ER to image a fault is also possible. If the fault has slipped sufficiently, then ER will be able to detect this change and image the fault.

The advantage of using the GPR in the Mississippi embayment region is its ease of deployment and the speed at which data can be gathered compared to ER. The total time to gather one 42 meter line of GPR data, including time to setup and unpack, is around 30 minutes. In contrast, the total time to gather a 42 meter ER line is about two hours, which is four times as long compared to the GPR. ER does have an advantage in that it is less affected by rainfall. Proof of this can be sees in figures 22 and 23 where rainfall was a significant hindrance at the Phenix site. Ideally, one would use both ER and GPR in combination as shown in figures 18, 19 and 20. The GPR can be used to recognizance the site, and point out which features are worth imaging with a different antenna or deploying ER over these locations.

As is illustrated by the results for the Morgan and Phenix sites, the optimal survey conditions for gathering GPR and ER data are in dry seasons of the year. This will minimize the negative effect of the zone of saturation. If substantial rainfall occurs, data collection would have to be delayed for many days. This is to allow time for the rain water to flow down below the water table. Another optimization condition is to be at a study site with no vegetation like grass, trees, crops, etc. This will eliminate the vegetation noise in the data from grassy spots as in figure 25 for the Morgan site B.

The optimal antenna would be in the range of 400 MHz to 250 MHz to image sand blows and faults that are no more than 2 to 8 meters deep, respectively. The optimal ER array is the same dipole-dipole array used in this study. This array is the best array to

image sand blows. It can also be used to image any other structure such as a fault because it has a good signal to noise ratio and it has sufficient depth penetration and horizontal resolution. When deploying this array for imaging a fault, the electrode spacing is the most important factor. If resolution is the main objective then the electrode separation will need to be as close as possible. However, if depth is the main objective then the electrode spacing needs to be further apart.

10. Conclusion

A combination of GPR and ER surveys has detected the presence of sand blows near the Morgan site and the Phenix site in southeastern Arkansas. A third GPR survey was conducted north of Montrose to detect the presence of a subsurface fault but site conditions proved to be unfavorable. The study indicated the strong influence of site conditions on the ability of the methods to detect sand blows. Optimal conditions involve dry soil and little reshaping of the ground surface for agricultural purposes. Optimal conditions were present during the Morgan site survey and the results provide the clearest evidence for sand blows. Despite less than optimal conditions at the Phenix site, several possible sand blow sites were revealed in a 3-D inversion of the ER data. Future use of ER and GPR will be beneficial in the search for other sand blows, particularly under optimal siting and weather conditions.

References

Al-Shukri, H. J., R. E. Lemmer, H. H. Mahdi, J. B. Connelly, 2005. Spatial and Temporal Characteristics of Paleoseismic Features in the Southern Terminus of the New Madrid Seismic Zone in Eastern Arkansas. Seismological Research Letters. 76, 502-11.

Cox, R.T., A.A. Hill, D. Larsen, T. Holzer, S.l Forman, T. Noce, C. Gardner, J. Morat, 2007. Seismotectonic Implications of Sand Blows in the Southern Mississippi Embayment. Engineering Geology. 89, 278-99.

Cox, R.T., Larsen, D., 2004. Investigation of seismically-induced liquefaction in the southern Mississippi Embayment. National Earthquake Hazard Reduction Program, Final Technical Report No. 03HQGR0011. U.S. Geological Survey, Reston, VA. 19 pp.

Cox, R.T., Larsen, D., Forman, S.L., Woods, J., Morat, J., Galluzzi, J., 2004. Preliminary assessment of sand blows in the southern Mississippi Embayment. Bulletin of the Seismological Society of America. 94, 1125–1142.

Cox, R.T., Van Arsdale, R.B., Harris, J.B., Forman, S.L., Beard, W., Galluzzi, J., 2000. Quaternary faulting in the southern Mississippi Embayment and implications for tectonics and seismicity in an intraplate setting. Geological Society of America Bulletin. 112, 1724–1735.

Hewitt, Edwin, Robert E. Hewitt, 1979. The Gibbs-Wilbraham Phenomenon: An Episode in Fourier Analysis. Archive for History of Exact Sciences. 21 (2), 129-60.

Jol, Harry M. 2009. Ground Penetrating Radar: Theory and Applications, 1st ed. Elsevier Science, Amsterdam, Netherlands.

Ogungbe, A. S., J. A. Olowofela, O. J. Da-Silva, A. A. Alabi, E. O. Onori, 2010. Subsurface Characterization Using Electrical Resistivity (Dipole-Dipole) Method at Lagos State University (LASU) Foundation School, Badagry. Advances in Applied Science Research. 1 (1), 174-81.

Reynolds, John M, 2011. An Introduction to Applied and Environmental Geophysics, 2nd Edition. John Wiley & Sons, United Kingdom.

Stummer, P., H. Maurer, A. G. Green 2004. Experimental Design: Electrical Resistivity Data Sets That Provide Optimum Subsurface Information. Geophysics. 69 (1), 120-39.

Szalai, S., Szarka, L., 2008. On the classification of surface geoelectric arrays. Geophysical Prospecting. 56 (2), 159-175.

Thomas, William A, 2006. Tectonic Inheritance at a Continental Margin. GSA Today 16 (2).

Tuttle, M.P., Al-Shukri, H., Mahdi, H., 2006. Very large earthquakes centered southwest of the New Madrid seismic zone 5,000—7,000 years ago. Seismological Research Letters. 77, 755–770.

Wolf, L.W., J. Collier, M. Tuttle, P. Bodin, 1998. Geophysical Reconnaissance of Earthquake-induced Liquefaction Features in the New Madrid Seismic Zone. Journal of Applied Geophysics. 39 (3), 121-29.